

## NEUTRINO-DRIVEN EXPLOSION OF A 20 SOLAR-MASS STAR IN THREE DIMENSIONS ENABLED BY STRANGE-QUARK CONTRIBUTIONS TO NEUTRINO-NUCLEON SCATTERING

TOBIAS MELSON<sup>1,2</sup>, HANS-THOMAS JANKA<sup>1</sup>, ROBERT BOLLIG<sup>1,2</sup>, FLORIAN HANKE<sup>1,2</sup>, ANDREAS MAREK<sup>3</sup>, AND BERNHARD MÜLLER<sup>4</sup>

*Draft version May 17, 2022*

### ABSTRACT

Interactions with neutrons and protons play a crucial role for the neutrino opacity of matter in the supernova core. Their current implementation in many simulation codes, however, is rather schematic and ignores not only modifications for the correlated nuclear medium of the nascent neutron star, but also free-space corrections from nucleon recoil, weak magnetism or strange quarks, which can easily add up to changes of several 10% for neutrino energies in the spectral peak. In the Garching supernova simulations with the PROMETHEUS-VERTEX code, such sophistications have been included for a long time except for the strange-quark contributions to the nucleon spin, which affect neutral-current neutrino scattering. We demonstrate on the basis of a  $20 M_{\odot}$  progenitor star that a moderate strangeness-dependent contribution of  $g_a^s = -0.2$  to the axial-vector coupling constant  $g_a \approx 1.26$  can turn an unsuccessful three-dimensional (3D) model into a successful explosion. Such a modification is well compatible with current experimental limits and reduces the neutral-current scattering opacity of neutrons, which dominate in the medium around and above the neutrinosphere. This leads to increased luminosities and mean energies of all neutrino species and strengthens the neutrino-energy deposition in the heating layer. Higher nonradial kinetic energy in the gain layer signals enhanced buoyancy activity that enables the onset of the explosion at  $\sim 300$  ms after bounce, in contrast to the model with vanishing strangeness contributions to neutrino-nucleon scattering. Our results demonstrate the close proximity to explosion of the previously published, unsuccessful 3D models of the Garching group.

*Subject headings:* supernovae: general — hydrodynamics — instabilities — neutrinos

### 1. INTRODUCTION

According to the standard paradigm of the explosion mechanism of core-collapse supernovae (SNe), neutrino heating above the gain radius initiates the outward acceleration of the stalled bounce shock and provides a major fraction of the energy that unbinds the explosion ejecta and powers the SN blast wave (e.g., Colgate & White 1966; Bethe & Wilson 1985; Bethe 1990; Janka 2012; Burrows 2013). Except for stars near the low-mass end of SN progenitors with oxygen-neon-magnesium cores or small iron cores and a steep density gradient of the overlying shells, successful explosions cannot be obtained in spherical symmetry (1D) by state-of-the-art simulations. For more massive progenitors the success of the neutrino-driven mechanism requires the support by multi-dimensional hydrodynamic flows in the postshock layer associated with convective overturn and the standing accretion shock instability (SASI; Blondin et al. 2003). Such flows increase the neutrino-energy deposition and create buoyancy and turbulent pressure, thus reducing the critical threshold for the neutrino luminosity to trigger the explosive runaway of the shock (e.g., Herant et al. 1994; Burrows et al. 1995; Janka & Müller 1996; Murphy & Burrows 2008; Nordhaus et al. 2010; Hanke et al. 2012; Dolence et al. 2013; Murphy et al. 2013). Breaking spherical symmetry also allows for simultaneous mass accretion and outflow from the proto-neutron star (PNS) after shock revival, which steepens the rise of the

explosion energy (Marek & Janka 2009).

The first self-consistent three-dimensional (3D) stellar core-collapse simulations with successful explosions were performed by Fryer & Warren (2002, 2004), using smoothed-particle hydrodynamics and a simple, grey diffusion description of neutrino transport, which favored rapid explosions in 2D and 3D. Recently, the Garching group has obtained a 3D explosion for a  $9.6 M_{\odot}$  star with a sophisticated, state-of-the-art ray-by-ray-plus (RbR+), multi-group transport solver and found that 3D hydrodynamic flows enhance the explosion energy compared to the 2D (axisymmetric) case (Melson et al. 2015). However, previous 3D simulations of this group for  $11.2$ ,  $20$ , and  $27 M_{\odot}$  progenitors had not produced explosions until  $\sim 400$ – $550$  ms after bounce, although corresponding 2D models had exploded (Hanke et al. 2013; Tamborra et al. 2013, 2014a,b). This is consistent with studies based on parametrized neutrino heating (e.g., Hanke et al. 2012; Couch 2013; Couch & O’Connor 2014; Couch & Ott 2015) and self-consistent simulations with approximate neutrino transport (Takiwaki et al. 2012, 2014), which revealed that the onset of explosion is less favored or delayed in 3D compared to 2D, contradicting claims by Nordhaus et al. (2010) and, though moderated, by Burrows et al. (2012) and Dolence et al. (2013). Also Mezzacappa et al. (2015), using high-fidelity RbR multi-group neutrino diffusion, highlight a successful  $15 M_{\odot}$  explosion that sets in significantly later than the corresponding 2D model. Large-scale deformation modes seem to have the strongest supportive effect on the explosion but are weakened by the forward turbulent energy cascade to small-scale structures in 3D, which is opposite to the 2D case.

While the resolution feasible in current full-scale 3D SN models is still insufficient to satisfactorily represent postshock turbulence (Abdikamalov et al. 2014; Radice et al. 2015), the results reported above suggest that important physics might

<sup>1</sup> Max-Planck-Institut für Astrophysik, Karl-Schwarzschild-Str. 1, 85748 Garching, Germany

<sup>2</sup> Physik Department, Technische Universität München, James-Franck-Str. 1, 85748 Garching, Germany

<sup>3</sup> Rechenzentrum der Max-Planck-Gesellschaft (RZG), Gießenbachstr. 2, 85748 Garching, Germany

<sup>4</sup> Monash Centre for Astrophysics, School of Physics and Astronomy, 9 Rainforest Walk, Monash University, VIC 3800, Australia

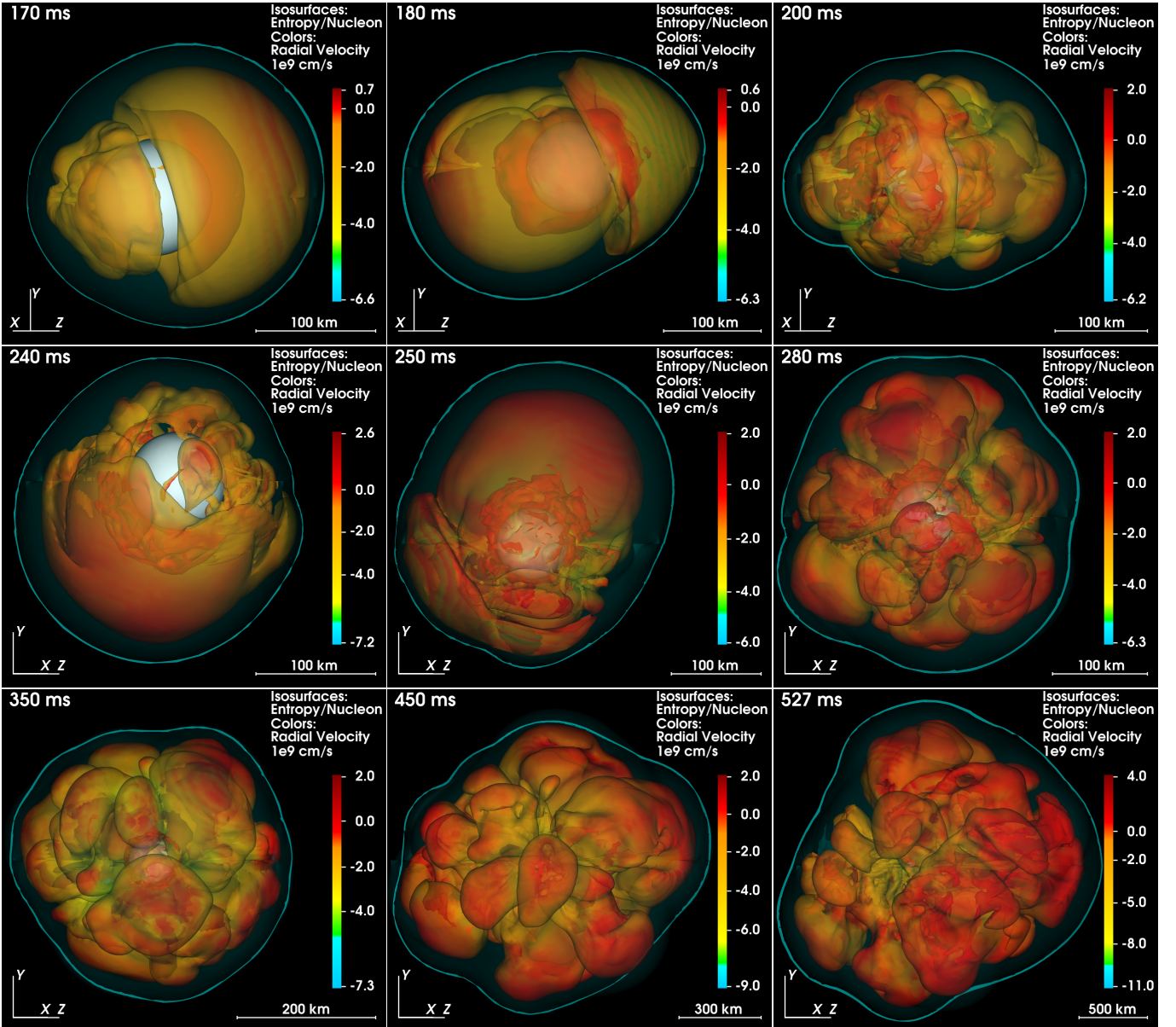


FIG. 1.— 3D iso-entropy surfaces for different times after bounce for exploding model 3Ds. Colors represent radial velocities. The supernova shock is visible by a thin surrounding line, the proto-neutron star by a whitish iso-density surface of  $10^{11} \text{ g cm}^{-3}$ . The yardstick indicates the length scale. Strong SASI activity occurs between  $\sim 120 \text{ ms}$  and  $\sim 280 \text{ ms}$ .

still be missing in the models. One of the aspects to be scrutinized are the pre-collapse initial conditions, which result from 1D stellar evolution modeling. Couch & Ott (2013), Couch et al. (2015), and Müller & Janka (2015) indeed confirmed long-standing speculations that large-amplitude perturbations of low-order modes in the convective shell-burning layers (e.g., Arnett & Meakin 2011, and references therein) might facilitate the development of explosions. Further progress will require 3D modeling of the final stages of stellar evolution.

Here we demonstrate that remaining uncertainties in the neutrino opacities, in particular the neutrino-nucleon interactions at subnuclear densities, can change the outcome of 3D core-collapse simulations qualitatively. As an example we consider possible strange-quark contributions to the nucleon spin in their effect on weak neutral-current scatterings. We show that a moderate isoscalar strange-quark contribution of

$g_a^s = -0.2$  to the axial-vector coupling constant  $g_a = 1.26$ , which is well within current experimental limits, suffices to convert our previous non-exploding  $20 M_\odot$  3D core-collapse run into a successful explosion.

We briefly describe our numerical approach in Sect. 2, summarize basic facts about the strange-quark effects in neutrino-nucleon scattering in Sect. 3, discuss our results in Sect. 4, and conclude in Sect. 5.

## 2. NUMERICAL SETUP AND PROGENITOR MODEL

We performed 2D and full ( $4\pi$ ) 3D simulations of a nonrotating, solar-metallicity  $20 M_\odot$  pre-SN progenitor (Woosley & Heger 2007).

We used the PROMETHEUS-VERTEX hydrodynamics code with three-flavor, energy-dependent, ray-by-ray-plus (RbR+) neutrino transport including the full set of neutrino reactions and microphysics (Rampp & Janka 2002; Buras et al. 2006) ap-

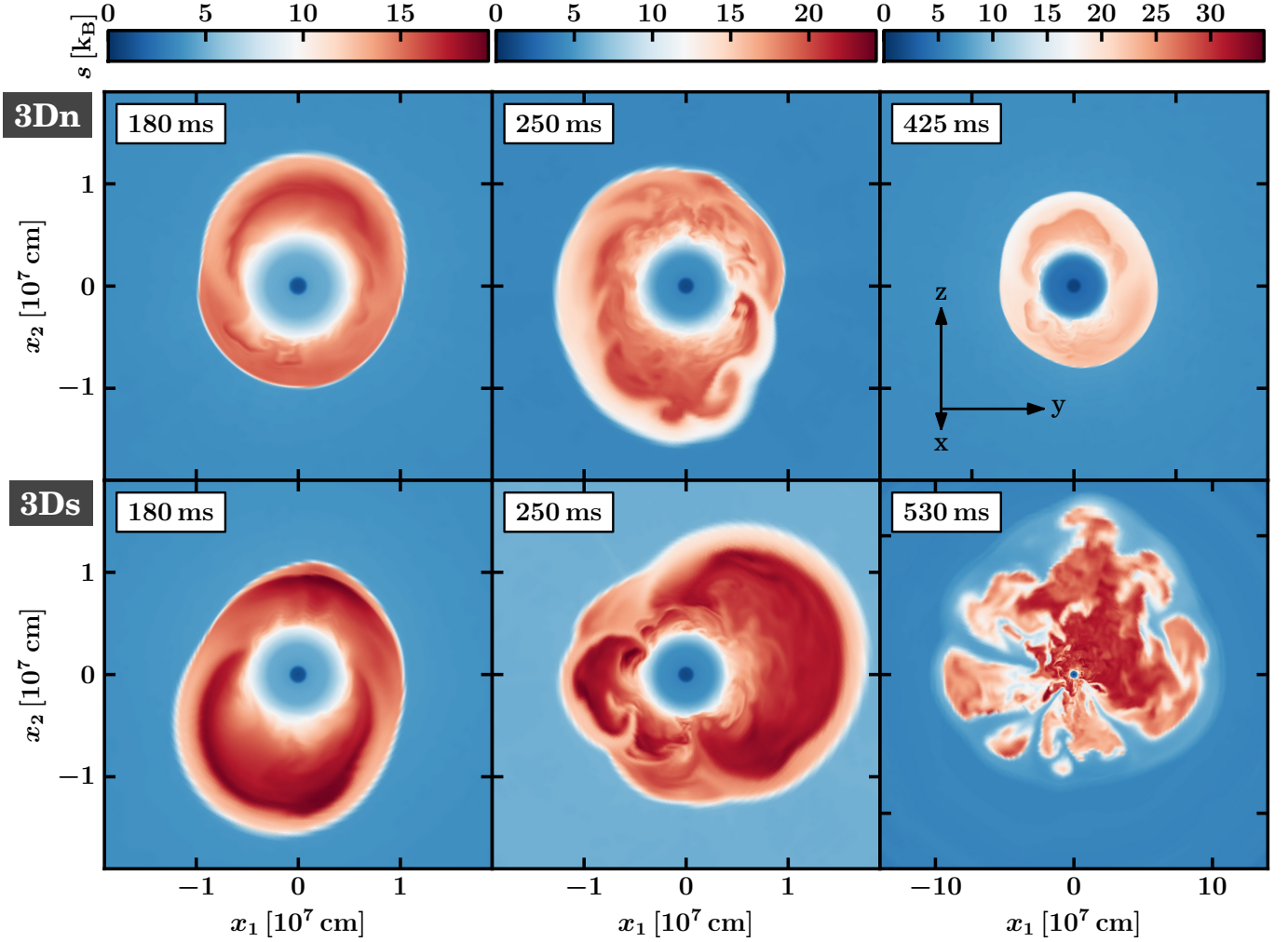


FIG. 2.— Cross-sectional entropy distributions (in  $k_B$  per nucleon) for the 3D models without (3Dn; upper row) and with strangeness contributions (3Ds; bottom). The bottom row clearly shows stronger SASI activity in model 3Ds (180 ms, 250 ms), whose traces are still imprinted on the ejecta geometry (530 ms) after the onset of the explosion (530 ms; note the different scale).

plied in 3D also by Hanke et al. (2013) and Tamborra et al. (2013, 2014a,b), in particular the high-density equation of state (EoS) of Lattimer & Swesty (1991) with a nuclear incompressibility of  $K = 220$  MeV. In order to avoid time-step constraints near the axis of the polar grid, the convectively stable central core with a radius of 10 km was computed in spherical symmetry. We used a 1D gravity potential (which is unproblematic for strongly PNS-dominated gravity fields) including general relativistic corrections (Marek et al. 2006). The radial grid had a reflecting boundary condition at the origin and an inflow condition at the outer boundary of  $10^9$  cm. It had 400 nonequidistant zones initially and was refined in steps up to  $>500$  zones, providing an increasingly better resolution of  $\Delta r/r \sim 0.01 \dots 0.004$  around the gain radius. For the neutrino transport 12 geometrically spaced energy bins with an upper bound of 380 MeV were used. The growth of non-radial hydrodynamic instabilities was seeded by imposing random cell-to-cell perturbations of 0.1% in density on the whole computational grid 10 ms after bounce.

### 3. STRANGENESS CONTRIBUTIONS TO NEUTRINO-NUCLEON SCATTERING

The lowest-order differential neutrino-nucleon scattering cross section reads

$$\frac{d\sigma_0}{d\Omega} = \frac{G_F^2 \epsilon^2}{4\pi^2} \left[ c_v^2 (1 + \cos \theta) + c_a^2 (3 - \cos \theta) \right], \quad (1)$$

with  $\epsilon$  being the incoming neutrino energy,  $\theta$  the scattering angle,  $G_F$  Fermi's constant, and  $c_v$  and  $c_a$  vector and axial-vector coupling constants, respectively. The latter are  $c_v = \frac{1}{2} - 2 \sin^2 \theta_W \approx 0.035$ ,  $c_a = g_a/2 \approx 0.63$  for  $\nu p \rightarrow \nu p$  and  $c_v = -\frac{1}{2}$ ,  $c_a = -g_a/2 \approx -0.63$  for  $\nu n \rightarrow \nu n$  with  $g_a \approx 1.26$  and  $\sin^2 \theta_W \approx 0.2325$ . For iso-energetic scattering ( $\epsilon' = \epsilon$ ), Eq. (1) yields the total transport cross section

$$\sigma_0^t = \int_{4\pi} d\Omega \frac{d\sigma_0}{d\Omega} (1 - \cos \theta) = \frac{2G_F^2 \epsilon^2}{3\pi} (c_v^2 + 5c_a^2). \quad (2)$$

While in our SN simulations corrections due to nucleon thermal motions and recoil, weak magnetism, and nucleon correlations at high densities are taken into account (Rampp & Janka 2002; Buras et al. 2006), Eqs. (1,2) provide good estimates. Strange quark contributions to the nucleon spin modify

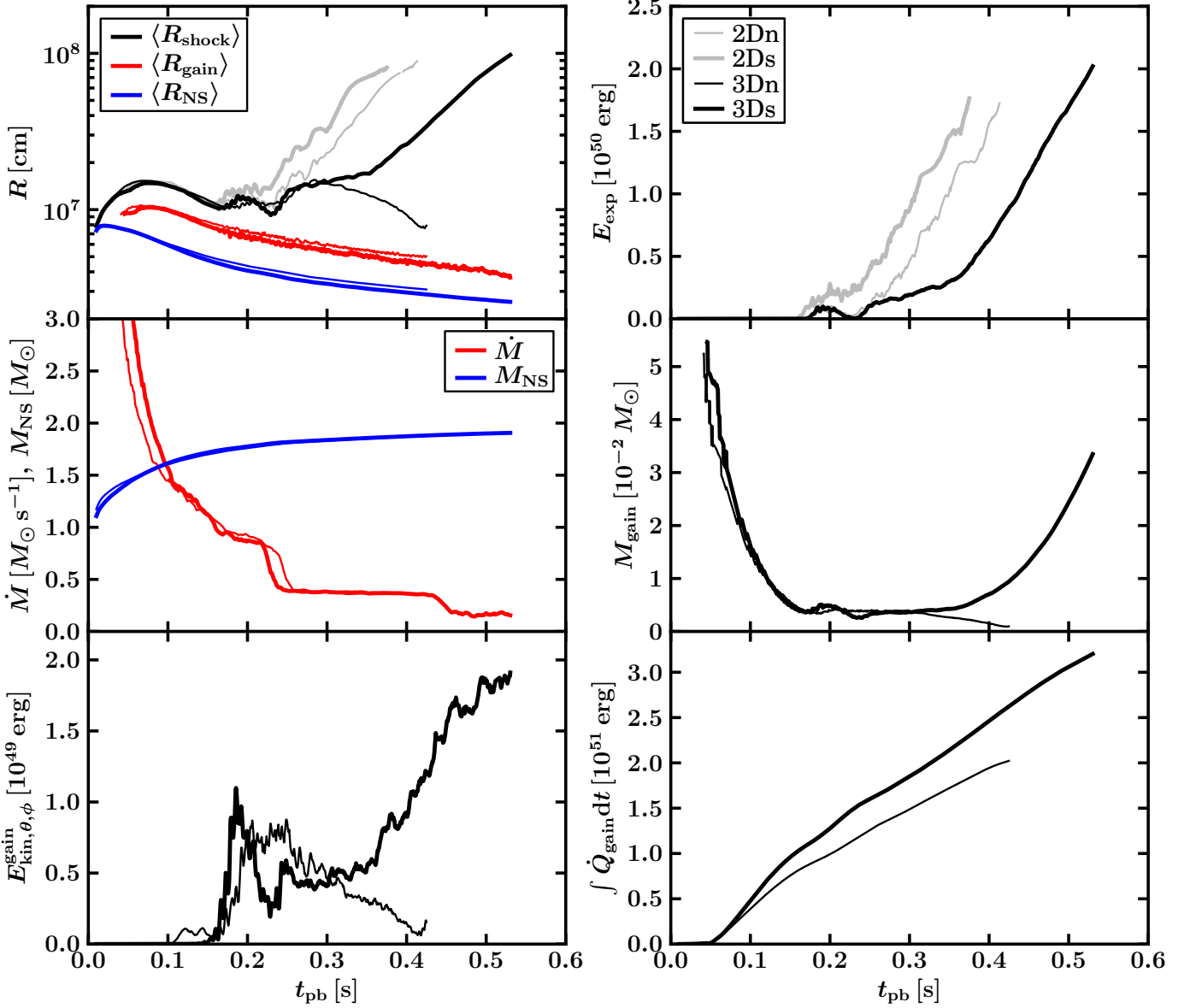


FIG. 3.— Explosion diagnostics for model 3Ds (thick lines) compared to the non-exploding model 3Dn (thin lines) as functions of post-bounce time  $t_{\text{pb}}$ . *Top left*: Angle-averaged shock radius (black), gain radius (red) and NS radius (blue; defined by a density of  $10^{11} \text{ g cm}^{-3}$ ); *top right*: diagnostic energy (positive total energy behind the shock). Gray lines display the corresponding 2D models without (2Dn, thin) and with strangeness contributions (2Ds, thick); *middle left*: mass-accretion rate ( $\dot{M}$ ) ahead of the shock (red) and baryonic NS mass (blue); *middle right, bottom left and right*: mass, non-radial kinetic energy, and time-integrated neutrino-energy deposition in the gain layer, respectively.

$c_a$  according to

$$c_a = \frac{1}{2} (\pm g_a - g_a^s), \quad (3)$$

where the plus sign is for  $\nu p$  and the minus sign for  $\nu n$  scattering (see, e.g., Horowitz 2002; Langanke & Martínez-Pinedo 2003). Since  $g_a^s \leq 0$ , the cross section for  $\nu p$ -scattering is increased and for  $\nu n$ -scattering decreased. The best current value of  $g_a^s = -0.15 \pm 0.09$  comes from  $\nu p$  elastic scattering experiments (Ahrens et al. 1987), but the correction could be considerably larger (e.g.,  $g_a^s = -0.4^{+0.5}_{-0.3}$  was recently concluded from MiniBooNE data; Golan et al. 2013).

Employing Eq. (2) with  $g_a^s = -0.2$ , Horowitz (2002) estimates 15, 21, 23% reduction of the neutral-current opacity for a neutron-proton mixture with electron fractions  $Y_e = 0.2, 0.1, 0.05$ , which are typical values for the layer between neutrinosphere (at density  $\rho \sim 10^{11} \text{ g cm}^{-3}$ ) and  $\rho \sim$

$10^{13} \text{ g cm}^{-3}$  for hundreds of milliseconds after bounce. Since strangeness does not affect charged-current interactions and NS matter is neutron-rich, the reduced scattering opacity allows mainly heavy-lepton neutrinos ( $\nu_x \equiv \nu_\mu, \bar{\nu}_\mu, \nu_\tau, \bar{\nu}_\tau$ ) to leave the hot accretion mantle of the PNS more easily. This was found to enhance the expansion of the stalled SN shock in 1D models, although not enough for successful shock revival (Liebendörfer et al. 2002; Langanke & Martínez-Pinedo 2003). However, below we will show that the situation can be fundamentally different in 3D simulations.

#### 4. RESULTS

We compare 2D and 3D core-collapse simulations of the  $20 M_\odot$  star with strangeness corrections in neutrino-nucleon scatterings, using  $g_a^s = -0.2$  (models 2Ds, 3Ds), to corresponding simulations without strange quark effects ( $g_a^s = 0$ ; models 2Dn, 3Dn) as in all SN simulations of the Garching

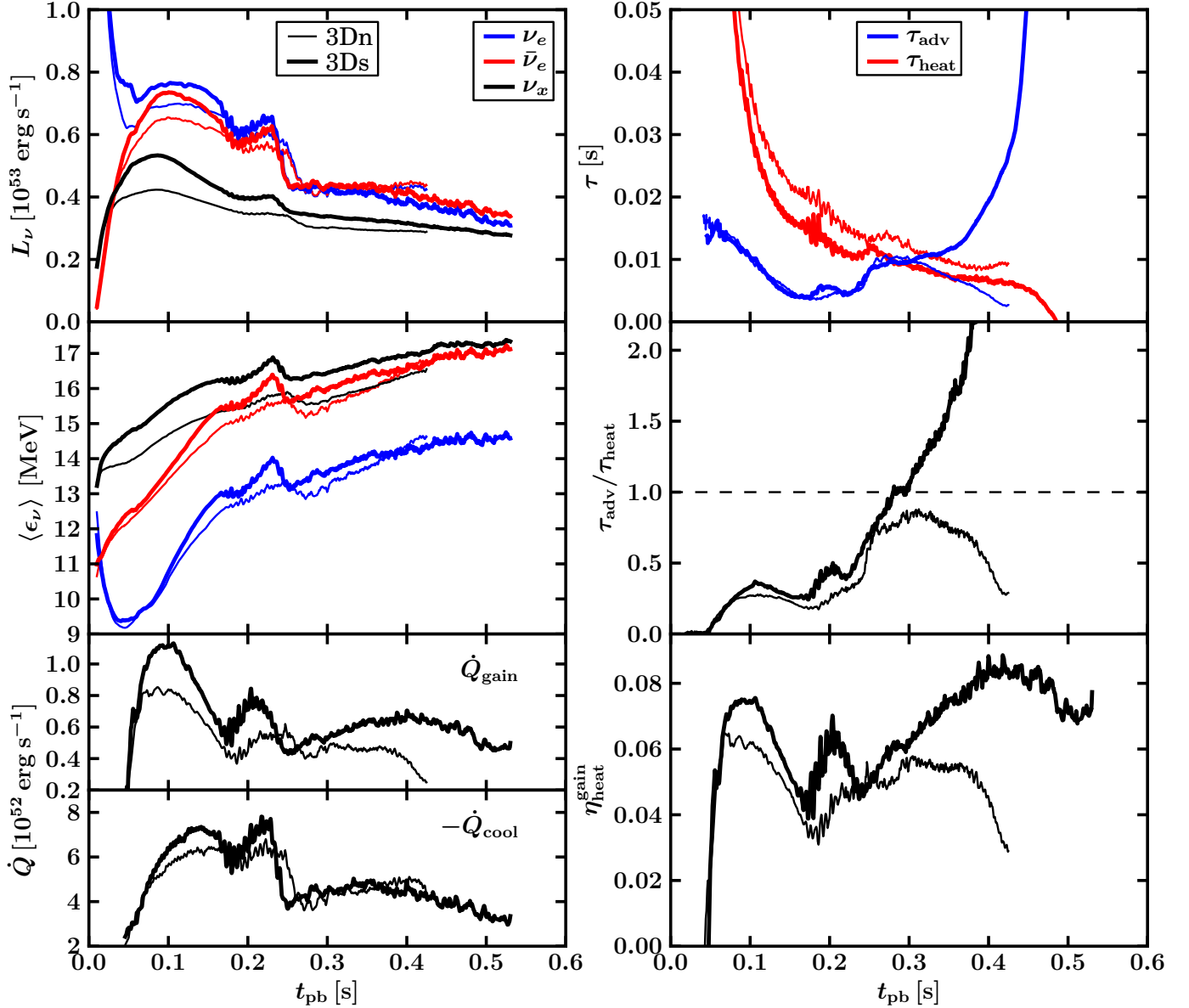


Fig. 4.— Neutrino-related quantities for model 3Ds (thick lines) compared to the non-exploding model 3Dn (thin lines) as functions of post-bounce time  $t_{\text{pb}}$ . Top and middle left: Neutrino luminosities and mean energies (defined as ratios of neutrino energy and number fluxes), respectively, for  $\nu_e$  (blue),  $\bar{\nu}_e$  (red), and one kind of  $\nu_x$  (black) for a distant observer at rest; bottom left: volume-integrated neutrino-energy deposition rate in the gain layer (upper panel) and cooling rate between NS radius and gain radius (lower panel); top, middle, bottom right: advection (blue) and heating time scale (red), corresponding time-scale ratio, and heating efficiency in the gain layer, respectively.

group so far.

#### 4.1. Dynamical evolution towards explosion

The sequence of 3D images in Fig. 1 shows the post-bounce evolution of the exploding model 3Ds; the entropy cuts in Fig. 2 demonstrate the differences to the unsuccessful model 3Dn. In both cases the dynamics of the accretion layer are strongly SASI-dominated. In model 3Ds there is no indication of postshock convection before SASI sloshing motions first appear at post-bounce (p.b.) time  $t_{\text{pb}} \sim 120$  ms. These reach full strength around 180 ms p.b. and continue in varying directions until  $\sim 280$  ms. Only later on convective overturn takes over as the dominant non-radial instability. In model 3Dn moderate buoyancy activity is visible from 100–180 ms before SASI becomes dominant, too. Early convection is enabled by a slightly larger radius of the stalled shock in 3Dn as a consequence of a slightly lower mass-accretion rate  $\dot{M}$

(Fig. 3). This difference improves the growth conditions for postshock convection. In 3Dn an erroneous change of the transition between low-density and high-density EoS caused a delay of the core collapse. Therefore the mass-accretion rate until  $t \sim 150$  ms is slightly reduced and the Si/Si+O interface arrives at the shock  $\sim 15$  ms later. These differences are inessential for our discussion.

From  $t_{\text{pb}} \sim 170$  ms on, 3Ds exhibits clearly larger SASI amplitudes and higher postshock entropies, which increases the maximum and average shock radii (Figs. 2, 3). This model also shows larger non-radial kinetic energies in the gain layer,

$$E_{\text{kin},\theta,\phi}^{\text{gain}} = \int_{\langle R_{\text{gain}} \rangle}^{R_{\text{shock}}(\theta,\phi)} dV \frac{1}{2} \rho (v_{\theta}^2 + v_{\phi}^2) \quad (4)$$

(Fig. 3), except during  $t_{\text{pb}} \sim 200$ –300 ms, when a powerful spiral SASI mode develops in model 3Dn but not in 3Ds, al-

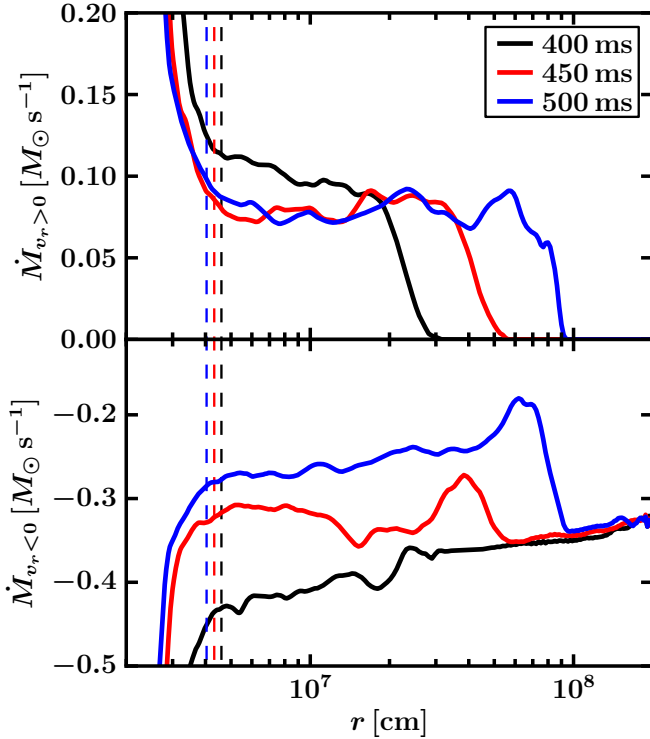


Fig. 5.— Total mass-accretion rate in inflows ( $v_r < 0$ ; top) and mass-outflow rate in rising plumes in the gain layer ( $v_r > 0$ ; bottom) at three times after the onset of explosion of model 3Ds. Vertical dashed lines mark the positions of the average gain radius, the steep forward edges indicate the average shock radii.

beit without pushing the shock sufficiently far out for revival (in conflict with recent results by Fernández 2015).

At  $t_{\text{pb}} \gtrsim 300$  ms, roughly 50 ms after the Si/Si+O interface has fallen through the shock and the shock has expanded to  $\sim 150$  km, the evolutions of models 3Dn and 3Ds separate. While in 3Dn the average shock radius,  $\langle R_{\text{shock}} \rangle$ , retreats again and conditions become unfavorable for an explosion, model 3Ds exhibits positive trends in all explosion-diagnostic parameters (e.g.,  $\langle R_{\text{shock}} \rangle$ ,  $E_{\text{kin},\theta,\phi}^{\text{gain}}$ ,  $M_{\text{gain}}$ ). Continuous shock expansion signals runaway and finally outward acceleration sets in at  $t_{\text{pb}} \gtrsim 360$  ms, at which time the recombination of free nucleons to  $\alpha$ -particles in the largest plumes begins to release energy and the instantaneous “diagnostic energy”,

$$E_{\text{exp}} = \int_{e_{\text{tot}} > 0, \text{postshock}} dV \rho e_{\text{tot}}, \quad (5)$$

starts to rise steeply, correlated with a fast growth of the mass in the gain layer (Fig. 3). In Eq. (5) the volume integration is performed over the postshock region where the total specific energy,

$$e_{\text{tot}} = e + \frac{1}{2}|\mathbf{v}|^2 + \Phi + [e_{\text{bind}}(^{56}\text{Fe}) - e_{\text{bind}}], \quad (6)$$

is positive, with  $e$ ,  $\frac{1}{2}|\mathbf{v}|^2$ , and  $\Phi$  being the specific internal, kinetic, and (Newtonian) gravitational energies. The bracketed term expresses the difference between the specific nuclear binding energy when all nucleons are finally recombined to iron-group nuclei compared to the nuclear composition at a given time. It therefore accounts for the maximum release of nuclear energy and corresponds to an upper limit of  $E_{\text{exp}}$ .

Both corresponding 2D models, 2Dn and 2Ds, also explode after the Si/Si+O interface has passed the shock, but in 2Ds

the outward shock acceleration and rise of  $E_{\text{exp}}$  sets in  $\sim 50$  ms earlier (Fig. 3). Strangeness corrections therefore create more favorable explosion conditions also in the 2D case, although their influence is modest in successful models, similar to their small effect in the 1D case, which is far away from explosion (Liebendörfer et al. 2002).

#### 4.2. Strangeness corrections and explosion

The impact of strangeness effects on the neutrino emission and the explosion is displayed in Fig. 4. Model 3Ds consistently exhibits higher luminosities and mean energies of the emission for all neutrino species, and, consequently, a higher neutrino-energy deposition rate in the gain layer,  $\dot{Q}_{\text{gain}}$ , a higher heating efficiency,

$$\eta_{\text{heat}}^{\text{gain}} = \frac{\dot{Q}_{\text{gain}}}{L_{\nu_e} + L_{\bar{\nu}_e}}, \quad (7)$$

a smaller gain radius (Fig. 3), and a shorter heating time scale,

$$\tau_{\text{heat}} = \frac{|E_{\text{gain}}|}{\dot{Q}_{\text{gain}}} \quad (8)$$

with  $E_{\text{gain}} = \int_{\langle R_{\text{gain}} \rangle}^{R_{\text{shock}}(\theta,\phi)} dV \rho (e + \frac{1}{2}|\mathbf{v}|^2 + \Phi)$  being the binding energy of the gain layer. Since the effective time scale of mass advection through the gain layer,

$$\tau_{\text{adv}} = \frac{M_{\text{gain}}}{\dot{M}} \quad (9)$$

(where  $\dot{M} > 0$ ), which measures the average exposure time of matter to neutrino heating, is very similar in models 3Ds and 3Dn, the smaller  $\tau_{\text{heat}}$  in 3Ds also leads to a higher time-scale ratio  $\tau_{\text{adv}}/\tau_{\text{heat}}$ . The ratio  $\tau_{\text{adv}}/\tau_{\text{heat}}$  exceeds the critical value of unity shortly before the SN shock in 3Ds begins its runaway.

The mean energies of the radiated neutrinos in model 3Ds are up to  $\sim 1$  MeV higher and the luminosities of  $\nu_e$  and  $\bar{\nu}_e$  by up to  $\sim 10\text{--}15\%$ , whereas the  $\nu_x$ -luminosities rise by up to  $\sim 30\%$ . The increase of the total neutrino luminosity is more than  $6 \times 10^{52}$  erg s $^{-1}$  at maximum, which mainly comes from layers below the  $\nu_e$ -sphere, because the neutrino-loss rate  $\dot{Q}_{\text{cool}}$  between the location of this sphere (at  $\sim 10^{11}$  g cm $^{-3}$ ) and the gain radius differs between models 3Ds and 3Dn by at most  $\sim 10^{52}$  erg s $^{-1}$  (Fig. 4). Note that at  $t_{\text{pb}} \gtrsim 300$  ms the relative differences of the neutrino properties of models 3Ds and 3Dn decrease and even change sign, because the former explodes whereas the latter continues to collapse and to accrete mass onto the PNS at a higher rate.

For  $Y_e = 0.1\text{--}0.05$ , strangeness effects in the neutrino-nucleon interactions reduce the effective opacity  $\kappa_{\text{eff}} = \sqrt{\kappa_{\text{abs}}(\kappa_{\text{abs}} + \kappa_{\text{scatt}})}$  for  $\nu_e$  only by 2–3% and for  $\bar{\nu}_e$  by 8–10%. A considerable part of the observed luminosity enhancement of  $\nu_e$  and  $\bar{\nu}_e$  is therefore caused indirectly by a stronger contraction of the PNS in response to the larger energy loss through  $\nu_x$  emission. With the smaller PNS radius (Fig. 3) and steeper density profile, the neutrinospheres of  $\nu_e$  and  $\bar{\nu}_e$  move inward to higher temperatures.

The reduction of the weak neutral-current scattering by strange quark contributions to the nucleon spin therefore enhances the neutrino luminosities and mean energies directly and indirectly and thus strengthens the neutrino heating in the gain layer. This amplifies buoyancy and turbulent mass motions behind the shock, which is signaled by higher non-radial

kinetic energy in model 3Ds at  $t_{\text{pb}} \gtrsim 300$  ms (Fig. 3), thus fostering the explosion of this model in contrast to 3Dn.

#### 4.3. Further development of explosion energy

At the final stage of the simulation at 530 ms p.b., the PNS has a baryonic mass of  $1.91 M_{\odot}$  and the shock has expanded to an average radius of  $\langle R_{\text{shock}} \rangle \approx 1000$  km. The diagnostic energy,  $E_{\text{exp}}$ , has reached  $0.2 \times 10^{51}$  erg and rises steeply and linearly with a rate of  $\dot{E}_{\text{exp}} \approx 1.2 \times 10^{51}$  erg s $^{-1}$ . This growth rate can be understood by the ejection of a continuous outflow of freshly neutrino-heated matter,  $\dot{M}_{v_r > 0} \sim 0.08\text{--}0.1 M_{\odot} \text{ s}^{-1}$  (Fig. 5; the subscript indicates positive radial velocity), which is mainly fed by the shock-accreted matter that is channeled to the gain radius in persistent accretion downdrafts (Fig. 2) with mass-inflow rates up to  $\sim 0.3 M_{\odot} \text{ s}^{-1}$  (Fig. 5). The mass outflow does not only absorb neutrino energy, it also releases nuclear binding energy from the recombination of neutrons and protons to  $\alpha$ -particles and heavy nuclei. Since neutrino heating roughly neutralizes the gravitational binding energy of the matter (Janka 2001; Marek & Janka 2009), the growth of  $E_{\text{exp}}$  can be estimated in terms of  $\dot{M}_{v_r > 0}$  and an average nuclear recombination energy per nucleon,  $\epsilon_{\text{nuc}}$ , as

$$\dot{E}_{\text{exp}} \approx \dot{M}_{v_r > 0} \frac{\epsilon_{\text{nuc}}}{m_B} \approx 1.2 \times 10^{51} \left( \frac{\epsilon_{\text{nuc}}}{6 \text{ MeV}} \right) \frac{\text{erg}}{\text{s}}. \quad (10)$$

To unbind the overlying layers of the progenitor with a gravitational binding energy of  $\sim 0.6 \times 10^{51}$  erg would therefore require massive outflow for several 100 ms. The neutrino-driven wind after the end of accretion as well as explosive nuclear burning will provide additional energy. For a reliable determination of the final SN explosion energy, model 3Ds would need to be evolved considerably longer than in our simulation.

#### 5. CONCLUSIONS

We have shown that strangeness contributions to neutrino-nucleon scattering with an axial-vector coupling of  $g_a^s = -0.2$  are sufficient to turn a non-exploding 3D simulation of a  $20 M_{\odot}$  model (in which  $g_a = 1.26$  was used for the standard isovector form factor) to a successful explosion. Strange-quark effects in the nucleon spin reduce the neutrino opacity of neutron-rich matter inside the neutrinosphere and thus directly and indirectly enhance the luminosities and mean energies of the radiated neutrinos. This leads to an amplification of the neutrino-energy deposition behind the stalled shock because charged-current interactions are not affected by nucleon strangeness. Owing to a reduced neutrino-heating time scale and stronger non-radial mass motions in the gain layer, the shock is driven to runaway expansion after the passage of the Si/Si+O interface. The enhanced neutrino emission enabled by the strangeness effects is associated with (and partly

caused by) a faster contraction of the PNS and a corresponding rise of the neutrinospheric temperatures. Strangeness corrections in neutrino-nucleon scattering are therefore similarly beneficial for shock revival as “softer” nuclear EoSs, which also lead to faster PNS contraction and stronger emission of more energetic neutrinos (Marek & Janka 2009; Janka 2012; Suwa et al. 2013).

Our results demonstrate how close previously published, unsuccessful 3D core-collapse models with the PROMETHEUS-VERTEX code were to explosion. They also underline that an accurate knowledge of neutrino-nucleon interaction rates, in particular also for neutral-current scattering, is of crucial importance for assessing the viability of the neutrino-driven explosion mechanism. While strangeness contributions affect neutrino-nucleon scattering everywhere, such opacity modifications between the subnuclear regime and neutrinospheric densities are most relevant for SN shock revival. In the discussed  $20 M_{\odot}$  simulations a modest  $\sim 15\%$  diminution of neutrino-neutron scattering makes all the difference between explosion and failure. Current experimental uncertainties of the isoscalar axial-vector form factor  $g_a^s$ , which is associated with strange-quark contributions to the nucleon spin, are well compatible with the value adopted in our study and might even point to larger effects. Better experimental constraints are highly desirable.

Nucleon-strangeness effects should also be investigated in 3D simulations of other progenitors. Moreover, our calculations must be repeated with better than  $2^{\circ}$  angular zoning to ensure that the explosion is robust and withstands higher angular resolution of the cascading of turbulent energy from the largest scales to small structures, which can be harmful for shock revival (Hanke et al. 2012; Couch 2013; Couch & O’Connor 2014; Abdikamalov et al. 2014). In any case, however, the outcome of multi-dimensional core-collapse simulations that marginally explode or fail can sensitively depend on effects on the 10% level in the neutral-current neutrino-nucleon interactions. This sensitivity needs to be taken into account in numerical implementations of these rates and might also be important for understanding partially conflicting model results published by different groups.

We thank Elena Erastova (RZG) for visualization support. At Garching, the project was funded by grant EXC 153 from DFG, ERC-AdG No. 341157-COCO2CASA, and computing time from the European PRACE Initiative on SuperMUC (GCS@LRZ, Germany) and MareNostrum (BSC, Spain). B.M. acknowledges support by ARC through DECRA grant DE150101145.

#### REFERENCES

Abdikamalov, E., Ott, C. D., Radice, D., Roberts, L. F., Haas, R., Reisswig, C., Moesta, P., Klion, H., & Schnetter, E. 2014, eprint arXiv:1409.7078

Ahrens, L. A., Aronson, S. H., Connolly, P. L., Gibbard, B. G., Murtagh, M. J., Murtagh, S. J., Terada, S., White, D. H., Callas, J. L., Cutts, D., Hoftun, J. S., Diwan, M., Lanou, R. E., Shinkawa, T., Kurihara, Y., Amako, K., Kabe, S., Nagashima, Y., Suzuki, Y., Tatsumi, S., Yamaguchi, Y., Abe, K., Beier, E. W., Doughty, D. C., Durkin, L. S., Heagy, S. M., Hurley, M., Mann, A. K., Newcomer, F. M., Williams, H. H., York, T., Hedin, D., Marx, M. D., & Stern, E. 1987, *PhRvD*, 35, 785

Arnett, W. D. & Meakin, C. 2011, *ApJ*, 733, 78

Bethe, H. A. 1990, *RvMP*, 62, 801

Bethe, H. A. & Wilson, J. R. 1985, *ApJ*, 295, 14

Blondin, J. M., Mezzacappa, A., & DeMarino, C. 2003, *ApJ*, 584, 971

Buras, R., Rampp, M., Janka, H.-T., & Kifonidis, K. 2006, *A&A*, 447, 1049

Burrows, A. 2013, *RvMP*, 85, 245

Burrows, A., Hayes, J., & Fryxell, B. A. 1995, *ApJ*, 450, 830

Burrows, A., Dolence, J. C., & Murphy, J. W. 2012, *ApJ*, 759, 5

Colgate, S. A. & White, R. H. 1966, *ApJ*, 143, 626

Couch, S. M. 2013, *ApJ*, 775, 35

Couch, S. M. & O’Connor, E. P. 2014, *ApJ*, 785, 123

Couch, S. M. & Ott, C. D. 2013, *ApJL*, 778, L7

Couch, S. M. & Ott, C. D. 2015, *ApJ*, 799, 5

Couch, S. M., Chatzopoulou, E., Arnett, W. D., & Timmes, F. X. 2015, eprint arXiv:1503.02199

Dolence, J. C., Burrows, A., Murphy, J. W., & Nordhaus, J. 2013, *ApJ*, 765, 110

Fernández, R. 2015, in preparation

Fryer, C. L. & Warren, M. S. 2002, *ApJ*, 574, 65

Fryer, C. L. & Warren, M. S. 2004, *ApJ*, 601, 391

Golan, T., Graczyk, K. M., Juszczak, C., Sobczyk, J. T. 2013, *PhRvC*, 88, 024612

Hanke, F., Marek, A., Müller, B., & Janka, H.-T. 2012, *ApJ*, 755, 138

Hanke, F., Müller, B., Wongwathanarat, A., Marek, A., & Janka, H.-T. 2013, *ApJ*, 770, 66

Herant, M., Benz, W., Hix, W. R., Fryer, C. L., & Colgate, S. A. 1994, *ApJ*, 435, 339

Horowitz, C. J. 2002, *PhRvD*, 65, 043001

Janka, H.-T. 2001, *A&A*, 368, 527

Janka, H.-T. 2012, *ARNPS*, 62, 407

Janka, H.-Th. & Müller, E. 1996, *A&A*, 306, 167

Langanke, K. & Martínez-Pinedo, G. 2003, *RvMP*, 75, 819

Lattimer, J. M., & Swesty, F. D. 1991, *NuPhA*, 535, 331

Liebendörfer, M., Messer, O. E. B., Mezzacappa, A., Hix, W. R., Thielemann, F.-K., & Langanke, K. 2002, in Proc. 11th Workshop on Nuclear Astrophysics, ed. W. Hillebrandt & E. G. M. Müller (München, Germany: Max-Planck-Institut für Astrophysik), 126

Marek, A. & Janka, H.-T. 2009, *ApJ*, 694, 664

Marek, A., Dimmelmeier, H., Janka, H.-T., Müller, E., & Buras, R. 2006, *A&A*, 445, 273

Melson, T., Janka, H.-T., & Marek, A. 2015, *ApJL*, 801, L24

Mezzacappa, A., Bruenn, S. W., Lentz, E. J., Hix, W. R., Harris, J. A., Bronson, M. O. E., Endeve, E., Chertkow, M. A., Blondin, J. M., Marronetti, P., & Yakunin, K. N. 2015, eprint arXiv:1501.01688

Müller, B. & Janka, H.-T. 2015, *MNRAS*, 448, 2141

Murphy, J. W. & Burrows, A. 2008, *ApJ*, 688, 1159

Murphy, J. W., Dolence, J. C., & Burrows, A. 2013, *ApJ*, 771, 52

Nordhaus, J., Burrows, A., Almgren, A., & Bell, J. 2010, *ApJ*, 720, 694

Radice, D., Couch, S. M., & Ott, C. D. 2015, eprint arXiv:1501.03169

Rampp, M. & Janka, H.-T. 2002, *A&A*, 396, 361

Suwa, Y., Takiwaki, T., Kotake, K., Fischer, T., Liebendörfer, M., & Sato, K. 2013, *ApJ*, 764, 99

Takiwaki, T., Kotake, K., & Suwa, Y. 2012, *ApJ*, 749, 98

Takiwaki, T., Kotake, K., & Suwa, Y. 2014, *ApJ*, 786, 83

Tamborra, I., Hanke, F., Müller, B., Janka, H.-T., & Raffelt, G. G. 2013, *PhRvL*, 111, 121104

Tamborra, I., Raffelt, G. G., Hanke, F., Janka, H.-T., & Müller, B., 2014a, *PhRvD*, 90, 045032

Tamborra, I., Hanke, F., Janka, H.-T., Müller, B., Raffelt, G. G., & Marek, A. 2014b, *ApJ*, 792, 96

Woosley, S. E.. & Heger, A. 2007, *PhR*, 442, 269